COBEM 2023 27TH INTERNATIONAL CONGRESS OF MECHANICAL ENGENEERING

ABCM Brazilian Society of Mechanical Sciences and Engineering
27th ABCM International Congress of Mechanical Engineering
December 04-08, 2023, Florianópolis-SC, Brazil

COB-2023-1573
VALIDATION OF A TIME-DOMAIN MODEL FOR ACOUSTIC IMPEDANCE TUBE DESIGN

Alexander Mattioli Pasqual
Thiago de Paula Sales
Aeronautics Institute of Technology, Division of Mechanical Engineering, Praça Mal. Eduardo Gomes 50, 12228-900, São José dos Campos, Brazil
apasqual@ita.br; tpsales@ita.br

Abstract. *The two-microphone impedance tube method is widely used in acoustic testing to obtain the absorption curves of materials. It consists in mounting two microphones at the tube wall, and placing a loudspeaker and a test specimen at the tube ends. Hence, the absorption curve is obtained by driving the loudspeaker with a broadband signal and processing the microphone signals. Although there are ASTM and ISO standards related to the impedance tubes, their proper design requires an in-depth knowledge to decide on the loudspeaker features, excitation signal, tube dimensions, microphone positions, signal processing techniques, and signal-to-noise ratio limits. To assist the impedance tube designer, a time-domain model that simulates the pressure signals has been developed and described in a previous paper. This model applies the finite element method to the one-dimensional wave equation, coupled to the Thiele-Small model of the loudspeaker. In this work, we present a validation of the model through experiments in a commercial tube with three microphone positions, so that two different spacings between sensors could be tested. Also, white and pink noise excitation signals were considered, with different signal-to-noise ratios and three test specimens. A comparison of the experimental and numerical results showed that the model is able to simulate the acoustic behavior of impedance tubes. Thus, it can be used as a tool for designing impedance tubes and testing signal processing techniques.*

Keywords: *acoustic testing, finite element method, sound absorption, signal processing.*

1. INTRODUCTION

Impedance tubes are widely used in acoustic testing to obtain the absorption and reflection curves of locally reactive materials under normal incidence. The most common experimental setup is the two-microphone method, which consists in flush mounting two microphones at two different positions in the tube side wall, and placing a loudspeaker and a test specimen at the tube ends. This method relies on broadband loudspeaker signals and benefits from modern digital signal processing techniques applied to the sound pressure signals sensed by the microphones.

The two-microphone impedance tube method was introduced a few decades ago (Seybert and Ross, 1977; Chung and Blaser, 1980; Bodén and Åbom, 1986) and is covered by ASTM and ISO standards (ASTM, 2019; ISO, 1998). Indeed, a number of manufacturers produce commercial impedance tube systems. However, many educational and research institutions have preferred to design and build their own systems (Suhanek *et al.*, 2008; Silva *et al.*, 2013; Ďuriš and Labašová, 2021). A proper design of impedance tubes requires an in-depth knowledge of its electroacoustic behavior to decide on the loudspeaker features, excitation signal, tube dimensions, microphone positions, signal processing techniques, and signal-to-noise ratio (SNR) limits. Also, the uncertainty analysis of the two-microphone method is a complex issue (Schultz *et al.*, 2007).

To shed light on these issues and to assist the impedance tube designer, the first author has developed a time-domain model that simulates the acoustic pressure signals the microphones would sense in a real experiment (Pasqual and Lara, 2017). This model makes use of the finite element method (FEM) to obtain a discrete version of the one-dimensional wave equation in the space domain, so that time numerical integration of the resulting set of ordinary differential equations leads to the desired sound pressure signals. The numerical procedure takes also into account the loudspeaker's electroacoustical behavior, and the boundary conditions at both ends of the tube. The common loudspeaker electroacoustic model described by Small (1972) is used, which is driven with pseudo-random signals in this paper. The boundary conditions correspond to the test specimen dynamical behavior and to the coupling between the loudspeaker and the acoustic wave.

In this work, we present a validation of the model by carrying out a set of experiments in a high-end commercial impedance tube. It has three holes to mount sensors, so that two different spacings between microphones could be tested. Also, white and pink noise excitation signals were considered, with different gains and SNRs to investigate whether the numerical model can predict errors related to measurement accuracy. In addition, three test specimens were considered: a rigid wall, an open-circuit loudspeaker acting as a passive absorber, and a short-circuit loudspeaker absorber.

The paper is organized as follows. Section 2 presents a review on the two-microphone method and the time-domain numerical model. Then, Section 3 describes the experimental and simulation procedures. In Section 4, the experimental and simulation results are presented and discussed. Finally, Section 5 summarizes the main results.

2. THEORY AND NUMERICAL MODELING

This section gives a brief overview on the two-microphone impedance tube method and the time-domain model used in the numerical simulations. For further details, the reader is referred to Pasqual and Lara (2017).

2.1 The two-microphone impedance tube method

Figure 1 shows a typical apparatus used to measure the acoustical properties of a test specimen by the two-microphone impedance tube method, where z is the spatial coordinate along the duct axis, L is the duct length, and $v(t)$ is the time-domain voltage signal applied to the loudspeaker voice-coil, which produces the sound pressure $p(z,t)$, $0 \leq z \leq L$, inside the duct. For plane wave propagation, $p(z,t)$ can be decomposed into an incident wave traveling in the $-z$ direction, $p_\mathrm{i}(t+z/c)$, and a reflected wave traveling in the $+z$ direction, $p_\mathrm{r}(t-z/c)$. Accordingly,

$$p(z,t) = p_\mathrm{i}(t+z/c) + p_\mathrm{r}(t-z/c) \underset{\mathcal{F}^{-1}}{\overset{\mathcal{F}}{\Longleftrightarrow}} P(z,\omega) = P_\mathrm{i}(0,\omega)\mathrm{e}^{\mathrm{j}kz} + P_\mathrm{r}(0,\omega)\mathrm{e}^{-\mathrm{j}kz}, \tag{1}$$

where $\mathcal{F}$ denotes the Fourier transform, $\mathrm{j} \equiv \sqrt{-1}$, $k = \omega/c$ is the wave number, ω is the angular frequency, and c is the sound speed.

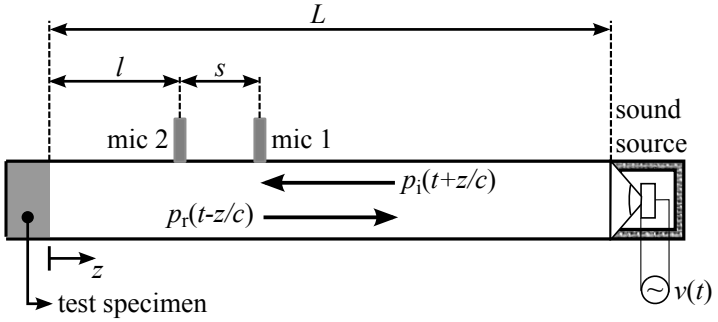

Figure 1. Schematic diagram of the two-microphone impedance tube method.

Let $H_{12}(\omega) \equiv P(l,\omega)/P(l+s,\omega)$ be the frequency response function (FRF) between the sound pressure signals sensed at two different positions, $z = l + s$ ("mic 1"), and $z = l$ ("mic 2"), as shown in Fig. 1. For stochastic excitation, $H_{12}(\omega)$ is given by (Shin and Hammond, 2008)

$$H_{12}(\omega) = \frac{G_{12}(\omega)}{G_{11}(\omega)}, \tag{2}$$

where G_{xx} is the one-sided power spectral density of a signal $x(t)$, and G_{xy} is the one-sided cross-spectral density of signals $x(t)$ and $y(t)$. The subscripts "1" and "2" refer to sound pressure signals at the positions "mic 1" and "mic 2", respectively. This FRF can also be expressed as

$$H_{12}(\omega) = \frac{H_{v2}(\omega)}{H_{v1}(\omega)} = \frac{G_{v2}(\omega)\big/G_{vv}(\omega)}{G_{v1}(\omega)\big/G_{vv}(\omega)}, \tag{3}$$

in which $H_{v2}(\omega)$ is the FRF between $v(t)$ and $p(l,t)$, and $H_{v1}(\omega)$ is the FRF between $v(t)$ and $p(l+s,t)$. Equation (3) is usefull when two non-synchronous measurements are carried out, using the same microphone and input channels, but with different microphone positions.

The reflection coefficient of the test specimen, $R(\omega)$, its sound absorption coefficient, $\alpha(\omega)$, and its specific acoustic impedance, $Z_\mathrm{s}(\omega)$, are related to $H_{12}(\omega)$ by the following set of equations (ASTM, 2019):

$$R(\omega) = \left[\frac{H_{12}(\omega) - \mathrm{e}^{-\mathrm{j}ks}}{\mathrm{e}^{\mathrm{j}ks} - H_{12}(\omega)}\right]\mathrm{e}^{\mathrm{j}2k(l+s)}, \tag{4}$$

$$\alpha(\omega) = 1 - |R(\omega)|^2, \tag{5}$$

and

$$\frac{Z_\mathrm{s}(\omega)}{\rho c} = \frac{1+R(\omega)}{1-R(\omega)}, \tag{6}$$

where ρ is the air density. Therefore, the acoustic properties can be evaluated from a proper estimation of $H_{12}(\omega)$. These relations hold only for plane wave propagation, which imposes an upper frequency limit for a given tube diameter, d. In addition, measurement accuracy imposes a lower frequency limit for a given spacing between microphones, s. According to ASTM (2019),

$$0.01\frac{c}{s} < f < 0.586\frac{c}{d}, \tag{7}$$

whereas ISO (1998) presents

$$0.05\frac{c}{s} < f < 0.58\frac{c}{d}. \tag{8}$$

This upper working frequency is a well-known result from the theory of sound propagation in cylindrical waveguides (Pierce, 1994), whereas the lower limit is just a recommendation, since it depends also on the SNR and the amount of damping of the test specimen (Pasqual and Lara, 2017).

2.2 Finite element modeling

The time-domain model used in this work is based on a FEM approximation of the one-dimensional wave equation, $\partial_{zz}p = (1/c^2)\partial_{tt}p$. Therefore, it holds for small-amplitude plane waves and neglects duct vibrations, as well as viscous and thermal losses. The finite element mesh is shown on the left of Fig. 2. It is made up of Q linear finite elements and $Q+1$ nodes, where L_q is the length of the qth element. The boundary conditions are modeled as damped mass-spring oscillators (see Fig. 2, on the right) representing the test specimen and the sound source. The latter is an electrodynamic loudspeaker driven by an electromagnetic force, $f_\mathrm{e}(t)$, given by (Small, 1972)

$$f_\mathrm{e}(t) = \frac{Bl_\mathrm{el}}{R_\mathrm{el}}\left[v(t) - Bl_\mathrm{el}\dot{\zeta}_\mathrm{l}(t)\right], \tag{9}$$

where Bl_el is the loudspeaker force factor, R_el is the voice-coil resistance, $\zeta_\mathrm{l}(t)$ is the diaphragm displacement, and $\dot{\zeta}_\mathrm{l}(t)$ is the diaphragm velocity.

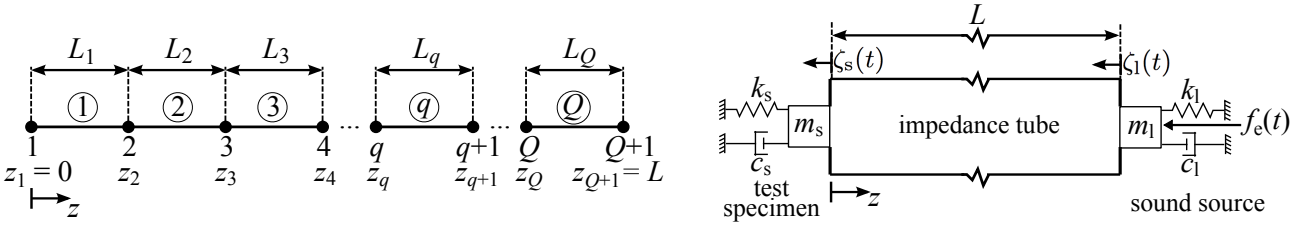

Figure 2. Finite element mesh (on the left) and simple oscillators as boundary conditions (on the right).

Let S, S_s, and S_d be the tube cross-sectional area, the net surface area of the test specimen, and the net surface area of the loudspeaker diaphragm, respectively. To couple the oscillators vibration to the acoustic waves, the following mass continuity conditions are used:

$$\dot{\zeta}_\mathrm{l}(t)S_\mathrm{d} = -u(L,t)S, \tag{10}$$

and

$$\dot{\zeta}_\mathrm{s}(t)S_\mathrm{s} = -u(0,t)S, \tag{11}$$

where $u(z,t)$ is the acoustic particle velocity. It is worth mentioning that Pasqual and Lara (2017) adopted $S = S_\mathrm{s} = S_\mathrm{d}$, which does not hold for the specimens tested in this work, as it will be seen in Section 3.

Let $\boldsymbol{\psi}(t) \equiv [\zeta_\mathrm{s}(t) \quad \tilde{\mathbf{p}}^\mathrm{T}(t) \quad \zeta_\mathrm{l}(t)]^\mathrm{T}$, where $\tilde{\mathbf{p}}(t)$ is a column vector containing the approximate sound pressure signals at the $Q+1$ nodes of the FEM mesh, and the superscript T indicates the transpose. The numerical model developed by Pasqual and Lara (2017) can be expressed as the following set of second-order ordinary differential equations:

$$\bar{\mathbf{M}}\ddot{\boldsymbol{\psi}}(t) + \bar{\mathbf{C}}\dot{\boldsymbol{\psi}}(t) + \bar{\mathbf{K}}\boldsymbol{\psi}(t) = \mathbf{b}v(t), \tag{12}$$

where $\bar{\mathbf{M}}$, $\bar{\mathbf{C}}$, and $\bar{\mathbf{K}}$ are square matrices of order $Q+3$ given by

$$\bar{\mathbf{M}} = \begin{bmatrix} & m_\mathrm{s} & & & \\ [\rho S_\mathrm{s}/S & 0 \cdots 0]^\mathrm{T}_{Q+1} & & \mathbf{M} & & [0 \cdots 0 & -\rho S_\mathrm{d}/S]^\mathrm{T}_{Q+1} \\ & 0 & & & & & m_\mathrm{l} \end{bmatrix}, \tag{13}$$

$$\mathbf{M} = \frac{1}{6c^2}\begin{bmatrix} 2L_1 & L_1 & 0 & \cdots & 0 & 0 \\ L_1 & 2L_1+2L_2 & L_2 & \cdots & 0 & 0 \\ 0 & L_2 & 2L_2+2L_3 & \cdots & 0 & 0 \\ \vdots & \vdots & \vdots & \ddots & \vdots & \vdots \\ 0 & 0 & 0 & \cdots & 2L_{Q-1}+2L_Q & L_Q \\ 0 & 0 & 0 & \cdots & L_Q & 2L_Q \end{bmatrix}, \tag{14}$$

$$\bar{\mathbf{K}} = \begin{bmatrix} & k_\mathrm{s} & & & \\ [0 & 0 \cdots 0]^\mathrm{T}_{Q+1} & & \mathbf{K} & & [0 \cdots 0 & 0]^\mathrm{T}_{Q+1} \\ & 0 & & & & & k_\mathrm{l} \end{bmatrix}, \tag{15}$$

$$\mathbf{K} = \begin{bmatrix} 1/L_1 & -1/L_1 & 0 & \cdots & 0 & 0 \\ -1/L_1 & 1/L_1+1/L_2 & -1/L_2 & \cdots & 0 & 0 \\ 0 & -1/L_2 & 1/L_2+1/L_3 & \cdots & 0 & 0 \\ \vdots & \vdots & \vdots & \ddots & \vdots & \vdots \\ 0 & 0 & 0 & \cdots & 1/L_{Q-1}+1/L_Q & -1/L_Q \\ 0 & 0 & 0 & \cdots & -1/L_Q & 1/L_Q \end{bmatrix}, \tag{16}$$

and the entries of the damping matrix $\bar{\mathbf{C}}$ are

$$\bar{C}_{ij} = \begin{cases} c_\mathrm{s}\ , & \text{if } i=j=1 \\ c_\mathrm{l} + \dfrac{(Bl_\mathrm{el})^2}{R_\mathrm{el}}\ , & \text{if } i=j=Q+3 \\ 0\ , & \text{otherwise} \end{cases}. \tag{17}$$

In addition, the entries of the column vector $\mathbf{b}$ are

$$b_i = \begin{cases} \dfrac{Bl_\mathrm{el}}{R_\mathrm{el}}\ , & \text{if } i=Q+3 \\ 0\ , & \text{otherwise} \end{cases}. \tag{18}$$

Equation (12) is a set of $Q+3$ coupled differential equations of second order. In this work, it is converted to a set of $2Q+6$ first-order differential equations (state-space formulation), which is suitable for numerical analysis, as described by Pasqual and Lara (2017).

3. METHODOLOGY

This section describes the experimental and simulation procedures related to the impedance tube measurements and the numerical modeling described in Section 2, respectively. In addition, the signal processing techniques we applied to the experimental and simulated data are briefly presented.

3.1 Experimental procedures

The experiments were carried out in the large tube ($d = 0.100$ m) of the Brüel & Kjaer type 4206 impedance tube kit with two different spacings between microphones, namely, $s = 0.050$ m and $s = 0.100$ m. The tube has three holes to mount the microphones, so that the spacing between microphones was set by changing the position of the "mic

1", whereas the position of the "mic 2" remained unchanged (see Fig. 1). Assuming $c = 343$ m/s, Equation (7) leads to $68 < f < 2010$ Hz, for $s = 0.050$ m, and $34 < f < 2010$ Hz, for $s = 0.100$ m. Equation (8) leads to $343 < f < 1989$ Hz, for $s = 0.050$ m, and $172 < f < 1989$ Hz, for $s = 0.100$ m. According to the manufacturer, the tube can be used in the frequency range from 50 Hz to 1.6 kHz.

Three different test specimens were evaluated: a rigid wall, an open-circuit passive loudspeaker absorber, and a short-circuit passive loudspeaker absorber. The rigid wall condition was obtained by using the sliding piston of the impedance tube kit. For the passive loudspeaker specimens, a 2-in Aurasound™ NSW2-326-8A driver was used, which was mounted in a circular baffle with 0.1 m of diameter to fit the inner tube dimension, as shown in Fig. 3. In addition, we let an air gap of 0.05 m between the back of the loudspeaker baffle and the sliding piston of the tube, leading to an air volume of $3.927 \cdot 10^{-4}$ m^3. All specimens were placed in the tube so that $l = 0.1$ m and $L = 0.5$ m.

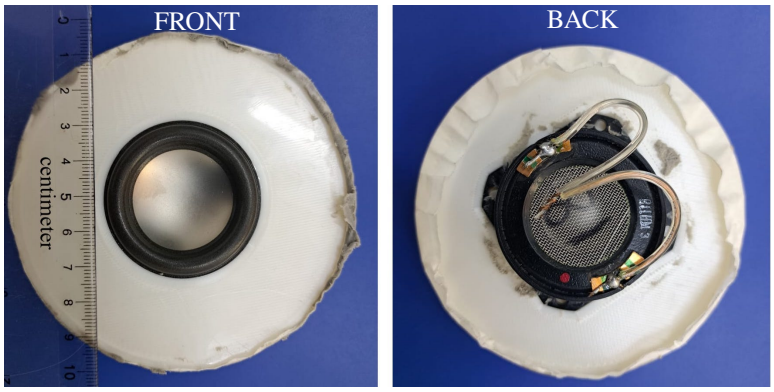

Figure 3. Loudspeaker (Aurasound™ NSW2-326-8A) mounted on a circular baffle with 0.1 m of diameter.

Two different kinds of test signals, with the same root mean square value, were used: white and pink noise. Both signals were band-limited from 40 Hz to 2.2 kHz, with duration of 50 s. They were generated in Matlab R2023a at 44,100 samples/s, and recorded as WAV audio files. During the experiments, the WAV file was played in a laptop and sent to the impedance tube source through the laptop analog audio output and a low cost audio amplifier. In addition, two different voltage gains were applied to investigate the effects of the SNR on the estimated absorption curves. The sound pressure signals were sensed by two ¼-in condenser microphones, Brüel & Kjaer type 4187, with preamplifiers Brüel & Kjaer type 2670, and microphone signal conditioners Brüel & Kjaer type 1780. These two signals, as well as the output voltage of the audio amplifier, were used as inputs to the data acquisition hardware, LMS SCADAS Mobile DB8-II, which was connected to a laptop running the LMS Test.Lab, as depicted in Fig. 4. In LMS Test.Lab, the acquisition sampling frequency and total time were set to 102,400 samples/s and 48.76 s, respectively.

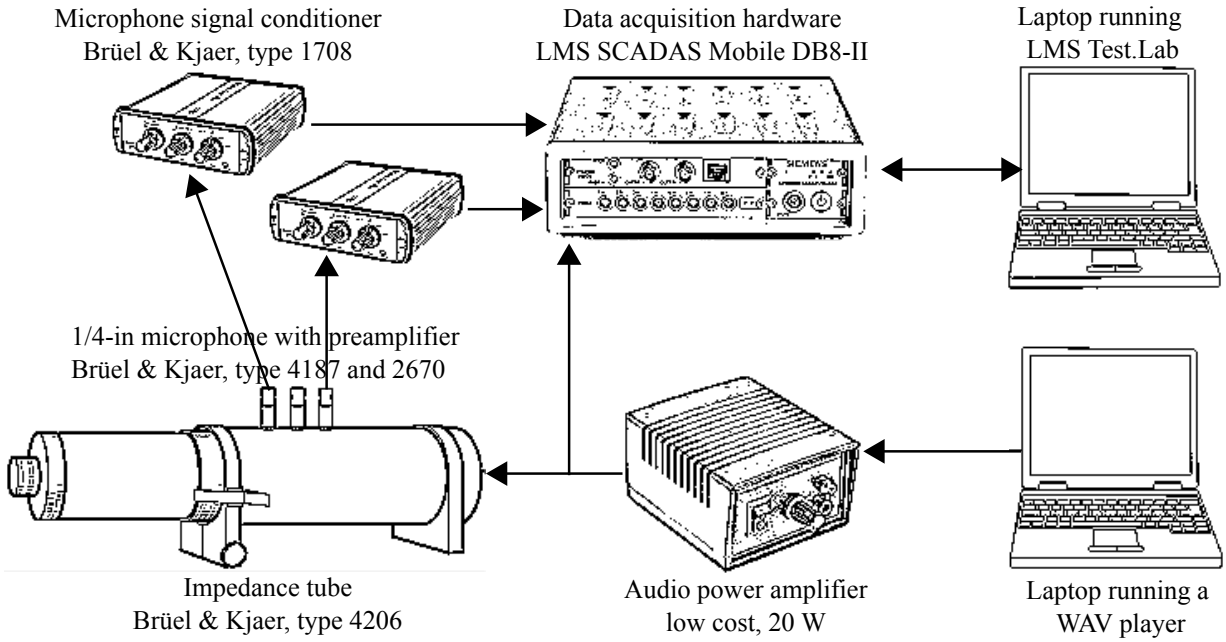

Figure 4. Layout for a three-channel signal acquisition: loudspeaker voltage and two microphones sound pressures.

Prior to each measurement, the pressure signals were recorded during 48.76 s at 102,400 samples/s with the audio

amplifier turned off, to estimate the background noise at each microphone position. In this paper, the SNR values refer to the power ratio between the experimental sound pressure and this recorded background noise. Because the position of "mic 2" was unchanged during the experiments, it has been used as a reference. Accordingly, the SNR will be referred to as "SNR_2".

3.2 Simulation procedures

The simulated sound pressure signals were obtained through numerical integration of Eq. (12) using the function "lsim" in Matlab R2023a and the same tube dimensions described in Section 3.1. To this end, such an equation was written in a standard state-space form, as presented by Pasqual and Lara (2017). A mesh made up of 100 finite elements of length 0.005 m was used. This yields 34.3 elements per wavelength at 2000 Hz, which is nearly the upper working frequency of the impedance tube. We let the loudspeaker voltage, $v(t)$, be the experimental voltage measured at the output terminals of the audio amplifier. In addition, each simulated pressure signal was polluted with additive noise, which was taken as the experimental pressure measured as background noise.

For all simulations, it was assumed that $c = 343$ m/s and $\rho = 1.21$ kg/m^3. Brüel & Kjaer provides no details on the impedance tube sound source, informing only that it is a 4-Ω loudspeaker, with 80 mm of diameter, and maximum average power of 10 W. Because of this lack of data, we assumed a Visaton™ FR-8 4-Ω loudspeaker, which is an 80-mm fullrange speaker with rated power of 10 W. From the Thiele-Small parameters given in its datasheet, one obtains $m_{\text{l}} = 1.6 \cdot 10^{-3}$ kg, $c_{\text{l}} = 0.2803$ N · s/m, $k_{\text{l}} = 6858.8$ N/m (including a closed-box volume of $2.3562 \cdot 10^{-4}$ m^3), $R_{\text{el}} = 3.4\ \Omega$, $Bl_{\text{el}} = 2.1$ T · m, and $S_{\text{d}} = 30 \cdot 10^{-4}$ m^2.

To simulate the passive loudspeaker absorber, we adopted the following parameters for the Aurasound™ NSW2-326-8A driver (Pasqual *et al.*, 2012): $m_{\text{s}} = 1.13 \cdot 10^{-3}$ kg, $c_{\text{s}} = 0.3079$ N · s/m, $k_{\text{s}} = 2440.6$ N/m (including a closed-box volume of $3.927 \cdot 10^{-4}$ m^3), $R_{\text{es}} = 6.29\ \Omega$, $Bl_{\text{es}} = 3.28$ T · m, and $S_{\text{s}} = 12.64 \cdot 10^{-4}$ m^2. The short-circuit condition was simulated by using $c_{\text{s}} + Bl_{\text{es}}^2/R_{\text{es}}$ instead of c_{s} in Eq. (17). The rigid wall specimen was simulated by letting $c_{\text{s}} = k_{\text{s}} = 0$, and $m_{\text{s}} = 10,000$ kg (Pasqual and Lara, 2017).

3.3 Signal processing

The experimental raw data and the simulated signals were processed in Matlab R2023a. The auto- and cross-power spectra were estimated by the Welch method, with Hanning-windowed blocks of 51,200 samples each (corresponding to time segments of 0.5 s), and 50% overlap between segments. The "H_1" estimator (Shin and Hammond, 2008) was used to obtain the FRFs described in Section 2.1. Then, for each experimental and simulated setup, the sound absorption curve was derived from the estimated H_{12} through Eqs. (4) and (5).

4. RESULTS

This section presents the simulation and experimental results for the three test specimens considered: rigid wall, open- and short-circuit passive loudspeaker absorber. The rigid wall is the most challenging specimen to be tested because it provides no damping ($\alpha = 0$), so that resonance peaks in the frequency response are very pronounced and pressure nodes strictly arise. Therefore — and for the sake of conciseness — we will present more results for the rigid wall specimen than for the passive loudspeaker absorber.

4.1 Rigid wall

Figure 5 shows experimental and simulated FRFs for two different setups. At the top row, we made $s = 0.050$ m and used a 0.0115-V_{rms} white noise as the test signal, which led to $\text{SNR}_2 = 19$ dB. The plots at the bottom row correspond to $s = 0.100$ m and a pink noise of 0.0768 V_{rms}, which led to $\text{SNR}_2 = 39$ dB. The minima and maxima of $|H_{v1}|$ and $|H_{v2}|$ correspond to pressure nodes and resonance frequencies, respectively. The latter are approximately the natural frequencies of a closed-closed tube rather than an open-closed one, which reveals that the mechanical impedance of the sound source plays an important role in the system behavior. The two frequencies corresponding to a pressure node at "mic 1" lead to the maxima of $|H_{12}|$, whereas the frequency corresponding to a pressure node at "mic 2" leads to the minimum of $|H_{12}|$. It can be noticed a good match between experimental and simulated results.

The absorption coefficient curves for the two configurations considered in Fig. 5 are shown at the top left and bottom right of Fig. 6. In addition, other four configurations are presented, with different combinations of test signals, spacing between microphones, and SNR. The theoretical curve ($\alpha = 0$) is also included for reference. Large errors might arise in the low-frequency range due to accuracy issues. Indeed, $H_{12} \to 1$ as $ks \to 0$ (see Fig. 5). Such errors can be reduced by increasing s and/or the SNR at low frequencies. The latter can be achieved by increasing the mean level of the test signal and/or by using a signal with more power in the low-frequency range, such as a pink noise. Figure 6 shows all these effects. For $s = 0.050$ m, small perturbations emerge at 572 and 1715 Hz. For $s = 0.100$ m, they occur at 430 and 1290 Hz. These perturbations arise because "mic 1" is at a pressure node for these frequencies.

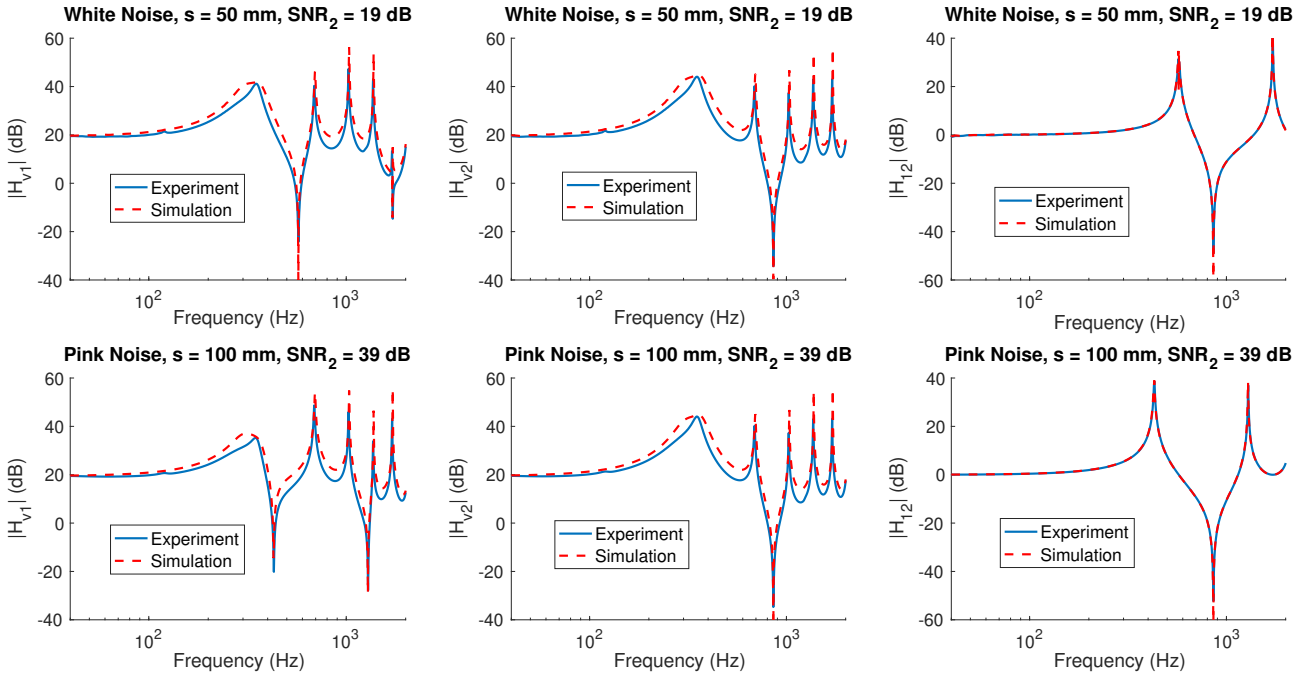

Figure 5. Experimental and simulated FRFs for the "rigid wall" specimen.

For this paper purposes, it is worth noting that the simulation results are able to reproduce the overall behavior of the errors in the low frequency range, as well as some perturbations related to microphones located at pressure nodes. On the other hand, the simulations do not capture the experimental curve behavior for $f > 1.6$ kHz with $s = 0.100$ m. This might be due to the onset of non-planar waves along the tube, which are not taken into account in the numerical model. Accordingly, the manufacturer of the impedance tube kit states that its upper frequency limit is 1.6 kHz.

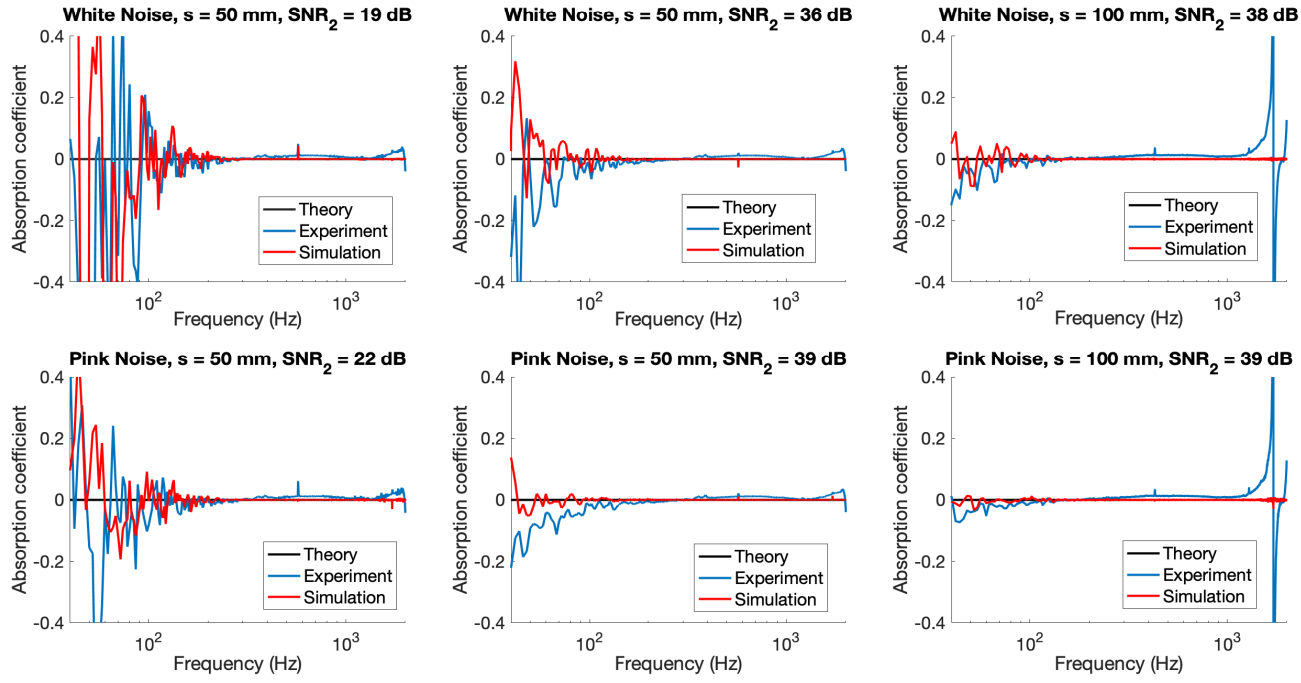

Figure 6. Theoretical, experimental, and simulated absorption coefficient curves for the "rigid wall" specimen.

4.2 Passive loudspeaker absorber

Figures 7 and 8 show theoretical, experimental, and simulated absorption coefficient curves for the open- and short-circuit loudspeaker absorber, respectively. For the sake of conciseness, we present only the results for pink-noise test signals. The theoretical curves were obtained from Eqs. (6) and (5) with $Z_s(\omega) = \{c_s + \mathrm{j}(m_s\omega - k_s/\omega)\}S/S_s^2$ for the open-circuit case, and $Z_s(\omega) = \{[c_s + (Bl_{es})^2/R_{es}] + \mathrm{j}(m_s\omega - k_s/\omega)\}S/S_s^2$ for the short-circuit case.

The absorption peak takes place near 230 Hz, which is the natural frequency of the specimen. Because the short-circuit condition increases the effective damping, the absorption peak is reduced, and the absorption curve spreads out towards lower and higher frequencies.

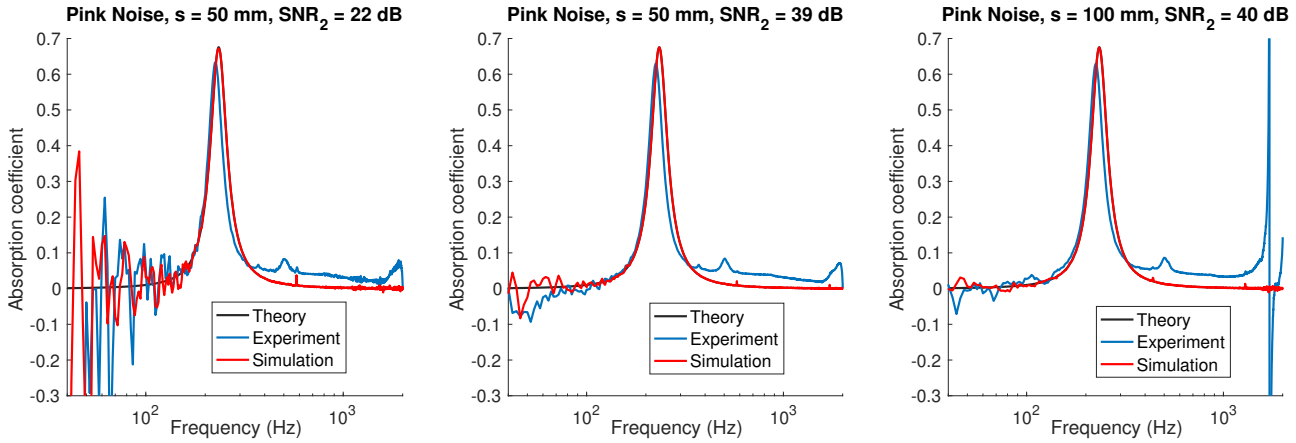

Figure 7. Theoretical, experimental, and simulated absorption coefficient curves for the open-circuit loudspeaker absorber.

The same low-frequency accuracy issues observed for the rigid wall specimen arise here, which are well captured by the simulations. Small perturbations due to microphones located at pressure nodes can also be observed at the same frequencies of the rigid wall specimen, as expected. Again, the simulations are not able to mimic the experimental curve behavior for $f > 1.6$ kHz with $s = 0.100$ m, which indicates the presence of non-planar waves.

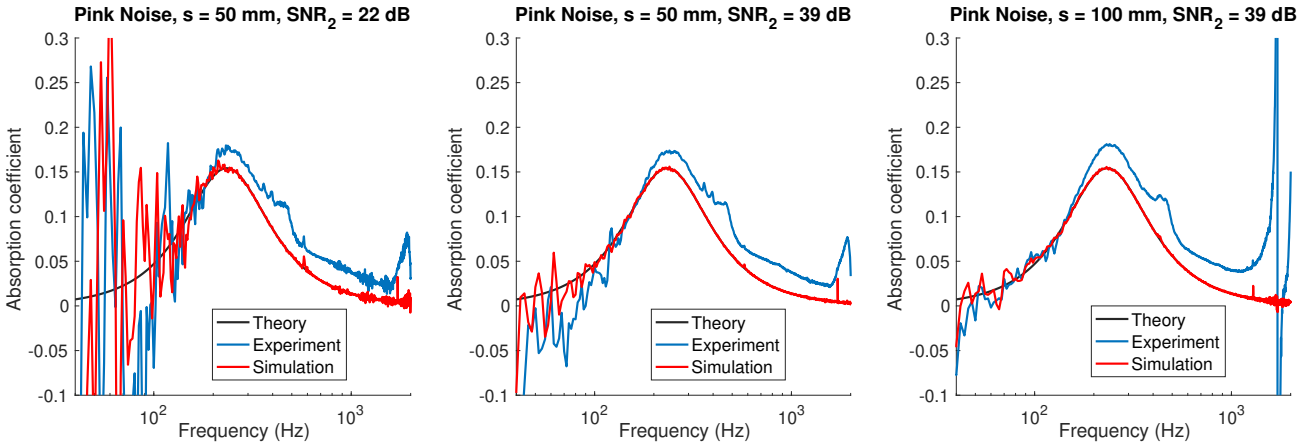

Figure 8. Theoretical, experimental, and simulated absorption coefficient curves for the short-circuit loudspeaker absorber.

If SNR is large enough, the theoretical and simulated absorption curves almost superimpose. However, the experimental curves present a larger absorption for frequencies above the specimen natural frequency, approximately. This might be due to dynamic features of the Aurasound™ NSW2-326-8A driver that were not modeled in the simulations, such as rocking modes and uneven diaphragm vibration. It is known that the diaphragm and surround suspension of this loudspeaker do not oscillate in phase for frequencies above 1.5 kHz (Pasqual *et al.*, 2010). This might explain the increased experimental absorption at those frequencies for $s = 0.050$ m.

5. CONCLUSIONS

This paper presented an experimental validation of a time-domain numerical model developed to assist the design of impedance tubes and to assess signal processing techniques. We conducted a set of experiments in a commercial impedance tube under different setups. Both white and pink noises were used as excitation signals, with two different

voltage gains, which aimed to evaluate whether the model is able to predict errors related to poor measurement accuracy. Simulations and experiments were carried out for three test specimens, namely, a "rigid wall", an open-circuit loudspeaker absorber, and a short-circuit loudspeaker absorber.

A comparison of experimental and simulated FRFs and absorption coefficient curves showed that the numerical model is able to reproduce the system behavior in the whole plane-wave frequency range. The low-frequency errors related to measurement accuracy were also captured by the model, as well as small perturbations at frequencies in which a microphone is located at a pressure node. On the other hand, the model was not able to mimic the errors for frequencies near the upper operational limit of the tube, probably due to the onset of non-planar waves. However, such a frequency can be easily predicted from a well-known analytical expression. Therefore, we conclude that the proposed numerical model can be used as a tool for designing impedance tubes and testing signal processing techniques.

6. ACKNOWLEDGEMENTS

This work was funded by FAPESP, São Paulo Research Foundation, under grant number 18/15894-0 (Research project: Periodic structure design and optimization for enhanced vibroacoustic performance, ENVIBRO).

7. REFERENCES

ASTM, 2019. "Standard test method for impedance and absorption of acoustical materials using a tube, two microphones and a digital frequency analysis system". ASTM E1050, American Society for Testing Materials, USA.

Bodén, H. and Åbom, M., 1986. "Influence of errors on the two-microphone method for measuring acoustic properties in ducts". *J. Acoust. Soc. Am.*, Vol. 79, No. 2, pp. 541–549.

Chung, J.Y. and Blaser, D.A., 1980. "Transfer function method of measuring in-duct acoustic properties: I. Theory". *J. Acoust. Soc. Am.*, Vol. 68, No. 3, pp. 907–913.

Ďuriš, R. and Labašová, E., 2021. "The design of an impedance tube and testing of sound absorption coefficient of selected materials". *IOP Conference Series: Materials Science and Engineering*, Vol. 1050, pp. 1–10.

ISO, 1998. "Acoustics – Determination of sound absorption coefficient and impedance in impedance tubes – part 2: Transfer-function method". ISO 10534-2, International Organization for Standardization, Switzerland.

Pasqual, A.M., Herzog, P. and Arruda, J.R.F., 2010. "Theoretical and experimental analysis of the electromechanical behavior of a compact spherical loudspeaker array for directivity control". *J. Acoust. Soc. Am.*, Vol. 128, No. 6, pp. 3478–3488.

Pasqual, A.M. and Lara, L.T., 2017. "Time-domain simulation of acoustic impedance tubes". *J Braz. Soc. Mech. Sci. Eng.*, Vol. 39, pp. 67–79.

Pasqual, A.M., Pachebat, M. and Herzog, P., 2012. "Influence of model parameter variability on the directivity filters of compact loudspeaker arrays". In *Proceedings of the Acoustics 2012 Nantes Conference*. Nantes, pp. 2845–2850.

Pierce, A.D., 1994. *Acoustics: An Introduction to its Physical Principles and Applications*, Acoustical Society of America, Melville, NY, chapter 7, pp. 313–370.

Schultz, T., Sheplak, M. and Cattafesta III, L.N., 2007. "Uncertainty analysis of the two-microphone method". *J. Sound Vib.*, Vol. 304, pp. 91–109.

Seybert, A.F. and Ross, D.F., 1977. "Experimental determination of acoustic properties using a two-microphone random-excitation technique". *J. Acoust. Soc. Am.*, Vol. 61, No. 5, pp. 1362–1370.

Shin, K. and Hammond, J.K., 2008. *Fundamentals of Signal Processing for Sound and Vibration Engineers*. John Wiley & Sons, Chichester, UK.

Silva, G.C.C., Nunes, M.A.A., Lopes, R.V. and Almeida Jr., A.B., 2013. "Design and construction of a low cost impedance tube for sound absorption coefficients measurements". In *Proceedings of the 22nd International Congress of Mechanical Engineering*. Ribeirão Preto, pp. 105–115.

Small, R.H., 1972. "Direct-radiator loudspeaker system analysis". *J. Audio Eng. Soc.*, Vol. 20, No. 5, pp. 383–395.

Suhanek, M., Jambrosic, K. and Domitrovic, H., 2008. "Student project of building an impedance tube". In *Proceedings of the 2nd ASA–EAA Joint Conference*. Paris, pp. 4477–4482.

8. RESPONSIBILITY NOTICE

The authors are solely responsible for the printed material included in this paper.